



Research



Cite this article: Medina JC, Warren E, Morgan D, Gow IE, Edwards J. 2024 Influence of Pd, Pt and Au nanoparticles in the photocatalytic performance of N-TiO₂ support under visible light. *Phil. Trans. R. Soc. A* **382**: 20230271. <https://doi.org/10.1098/rsta.2023.0271>

Received: 4 June 2024

Accepted: 29 July 2024

One contribution of 12 to a discussion meeting issue 'Green carbon for the chemical industry of the future'.

Subject Areas:

materials science, nanotechnology, physical chemistry

Keywords:

water pollution, visible light absorption, metallic nanoparticles

Author for correspondence:

Jennifer Edwards

e-mail: edwardsjk@cardiff.ac.uk

Influence of Pd, Pt and Au nanoparticles in the photocatalytic performance of N-TiO₂ support under visible light

J. C. Medina, Eleanor Warren, David Morgan, Isla E. Gow and Jennifer Edwards

Cardiff Catalysis Institute, Cardiff University School of Chemistry, Translational Research Hub, Cardiff University, Maindy Road, Cardiff CF24 4HQ, UK

JE, 0000-0003-4089-2827

In this article, we report the modification and photocatalytic evaluation of commercial TiO₂-P25 under visible light for methyl orange (MO) dye degradation under visible light. The activity of materials doped with N, Pd, Pt and Au on to the TiO₂-P25 was evaluated, with optimal photocatalytic performance achieved using Au nanoparticles doped on an N-functionalized titania surface. X-ray diffraction (XRD), physical nitrogen adsorption/desorption isotherm curves, transmission electron microscopy (TEM), diffuse reflectance spectroscopy, scanning electron microscopy (SEM) and energy dispersive X-ray spectroscopy (EDX) were used to study the structural and textural properties of the samples. The chemical species present in the bulk and surface of the catalysts were identified using X-ray photoelectron spectroscopy (XPS) and microwave plasma-atomic emission spectroscopy. The results show that Au/N-TiO₂ photocatalyst presents a remarkable enhanced activity for MO dye degradation, under visible light illumination, reaching 100% after 4 h. The enhanced photocatalytic activity using this composite is attributable to the well-dispersed and small size of Au nanoparticles, large surface area, reduction of band-gap energy and the interaction between nitrogen and Au which promoted a synergistic effect.

© 2024 The Author(s). Published by the Royal Society under the terms of the Creative Commons Attribution License <http://creativecommons.org/licenses/by/4.0/>, which permits unrestricted use, provided the original author and source are credited.

1. Introduction

A viable solution providing a renewable and sustainable energy source with the potential to meet continually growing energy demands, as well as the remediation of environmental pollutants can be achieved using photocatalysis. Synthetic dyes are widely employed in the textile industry, posing a significant environmental challenge when disposed of into effluents. Because synthetic dyes are complex, traditional biological treatments cannot effectively achieve both discolouration and wastewater degradation. In recent decades, there has been a surge of interest in advanced oxidation processes as a more efficient approach for eliminating aqueous and gaseous pollutants. Numerous studies have highlighted the photocatalytic activity of oxide semiconductors for oxidizing organic compounds in residual water. Since the seminal work of Fujishima & Honda [1], discussing hydrogen-photo-electrochemical production, titanium dioxide has been extensively utilized as photocatalyst, thanks to its chemical stability, durability, minimal toxicity and favourable production capacity. Furthermore, the high density of states in its bands allows TiO₂ to efficiently convert photons to current, thereby enhancing its photocatalytic activity beyond that of other semiconductors [2]. However, for its large band gap of 3.2 eV, a TiO₂ photocatalyst is only effective when irradiated by UV light (comprising only 5% of the solar spectrum), but the most significant impediment to its practical deployment is the quick recombination of its photogenerated electron-hole pairs [3]. This has resulted in many approaches to improve the catalytic activity, including the addition of metal-oxide heterojunctions [4], non-metal element doping [5] and noble-metal doping [6]. Furthermore, it has been demonstrated that a number of variables, including the concentration of the photocatalyst, the pH of the dye solution, the presence of oxidants and the light intensity, affect how quickly azo dyes photodegrade [7]. Therefore, modification of pH, addition of inorganic oxidants [8] (O₃ or H₂O₂) or use of powerful UV light illumination sources are procedures commonly employed to obtain high degradation efficiencies.

The use of noble metals (Au, Ag, Rh and Pd) has shown to be an effective way to change physical parameters such as absorption edge, crystallite size, surface area and charge transfer process. Doping the surface of TiO₂ with noble metals such as Ag [9], Au [10–12], Pt [13] and Pd [14,15] has been largely investigated by several researchers and shown to increase photocatalytic activity under visible light by acting as an electron trap, thereby augmenting the rates of photo-induced electron transfer at the interface. Additionally, they play a role in inhibiting the recombination of electron-hole pairs. The Fermi levels associated with TiO₂ are higher than those for noble metals, and significant reductions in electron-hole recombination rates are seen by incorporating TiO₂ with noble-metal dopants. Kim *et al.* [13] showed that photogenerated electrons become trapped upon modifying TiO₂ with Pt, thus promoting interfacial charge transfer rates. Seery *et al.* [16] reported that Ag-modified TiO₂ can extend the photo response of TiO₂ towards visible light. During dye degradation studies, the addition of Ag was found to enhance the degradation rates of rhodamine 6G dye. In the same study, Ag⁺ ions were found to enhance the visible light absorption capacity of the TiO₂ material by limiting the recombination rates of photogenerated electrons/holes. Camposeco *et al.* [17] reported a remarkable enhancement of photocatalytic activity in the water-splitting reaction to produce H₂, where the presence of metallic nanoparticles improved the photocatalytic activity of TiO₂ nanotubes. Recently, Motamedisade *et al.* [18] presented a novel catalyst for dye degradation fabricated with Au nanoclusters on nitrogen-functionalized TiO₂. Clark *et al.* [19] have improved the selectivity of methyl orange (MO) and 4-chlorophenol degradation relative to TiO₂ by using a distorted perovskite structure, CaCu₃Ti₄O₁₂. The use of square planar Cu²⁺ and octohedral Ti⁴⁺ sites

generates two individual band gaps. Recombination rate is decreased because an electron–hole trap is formed between localized Cu^+ sites and the conduction band in Ti^{3+} .

On the other hand, nitrogen-doped titania has gained significant attention in the field of photocatalysis. Numerous studies have identified it as a promising material for various environmental applications [20–22]. Characteristic features of nitrogen atoms, such as small ionization energy, similar atomic size and high stability compared to oxygen, encourage the incorporation of nitrogen dopants into the structure of TiO_2 [22,23]. Upon incorporation of nitrogen impurities into the TiO_2 material, the energy associated with oxygen vacancies decreases from 4.2 to 0.6 eV, thus nitrogen dopants favour oxygen vacancy formation [24]. This doping enhances the material's photocatalytic efficiency by narrowing the band gap, allowing better utilization of visible light. Furthermore, nitrogen attached to the surface can serve as active sites, forming strong complexes between metallic nanoparticles and titania surfaces. This interaction increases the loading level of the nanoparticles and reduces their agglomeration [18], thereby enhancing the overall photocatalytic efficiency and stability of the material.

It is clear that the use of non-metals and metals on the surface of titania helps to enhance its photocatalytic performance in photocatalytic reactions. In this article, we show the synthesis of modified TiO_2 photocatalysts for MO dye degradation. The aim was to evaluate the effect of three different metals on nitrogen-functionalized TiO_2 support (Pd/N-TiO_2 , Pt/N-TiO_2 and Au/N-TiO_2) and its influence on the MO dye degradation under visible light illumination.

2. Experimental details

(a) Photocatalyst synthesis

(i) N-doped TiO_2 support

Hexamethylenetetramine (HMT), $\text{C}_6\text{H}_{12}\text{N}_4$ (Sigma-Aldrich) was used as the nitrogen source. Manual grinding of TiO_2 powder P25 (Degussa) and HMT was performed for 15 min using a pestle and mortar. The amount of HMT was 20 wt% and the sample was identified as N- TiO_2 . The resultant N-doped TiO_2 was calcined at 400°C for 1 h in flowing air with a ramp rate of 5°C min^{-1} .

(ii) Addition of metallic nanoparticles to N- TiO_2 support

Gold, platinum and palladium nanoparticles were added to the N-doped TiO_2 support by deposition–precipitation with the urea (DPU) method in the absence of light. The target metal concentration was 1 wt%. The metal precursors were hydrogen tetrachloroaurate (III) hydrate ($\text{HAuCl}_4 \cdot 3\text{H}_2\text{O}$), potassium tetrachloroplatinate (K_2PtCl_4), palladium nitrate hydrate $\text{Pd}(\text{NO}_3)_2 \cdot 2\text{H}_2\text{O}$ and urea (0.42 M), all supplied by Sigma-Aldrich. In all cases, the metal precursor and urea were dissolved in 20 ml of distilled water. Then, 500 mg of N- TiO_2 (obtained by manual grinding) was added to the solution; subsequently, the suspension was vigorously stirred at 80°C for 16 h.

After the DPU method was completed, all materials were filtered, washed with distilled water and dried at 80°C for 12 h. Following drying, the samples were vacuum-sealed and kept at room temperature in a desiccator, shielded from light, to prevent any alterations.

All samples underwent thermal activation treatments under H_2 at 400°C for 2 h with a ramp rate of 5°C min^{-1} .

(b) Characterization techniques

The crystalline structure of the materials was studied using X-ray diffraction (XRD) and a PANalytical X'pert Pro powder diffractometer operating at 40 kV, 40 mA using $\text{Cu K}\alpha$ radiation

($\lambda = 1.54 \times 10^{-10}$ m) with a Ge (111) single crystal monochromator. The phases present were assigned using the International Centre for Diffraction Data database as a reference. Transmission electron microscopy (TEM) analysis was conducted using a JEOL JEM-2100 operating at 200 kV. Powders were deposited on to 300 mesh copper grids coated with holey carbon film for imaging. Scanning electron microscopy (SEM) was performed on a Tescan Maia3 field emission gun microscope. An Oxford Instruments XMAX^N 80 energy dispersive X-ray (EDX) detector was used for elemental analysis, controlled by Aztec software. The samples were dispersed as powders on to adhesive carbon Leit discs fixed to 12.5 mm aluminium stubs. For imaging purposes, the samples were coated with a 10 nm coating of 80:20 Au:Pd atoms by a Quorum plasma coater to prevent charging, and images were acquired using the secondary electron detector. The uncoated samples were analysed for EDX using the backscattered electron detector. The optical properties of the photocatalysts were measured using a UV–vis spectrometer, CARY 4000, equipped with a Harrick Praying Mantis attachment.

The textural properties were obtained using a Quantachrome Nova 2200E. A Brunauer–Emmett–Teller (BET) equation based on N₂ physisorption data was used to determine the specific surface area. The Barrett–Joyner–Halenda method was applied to calculate the pore size distribution from the desorption branch of the isotherm. The materials were dried for 4 h at 100°C and outgassed prior to nitrogen adsorption. The chemical composition of the materials was analysed on a Thermo Fisher Scientific K-Alpha⁺ photoelectron spectrometer utilizing micro-focussed monochromatic Al K α radiation operating at 72 W power (6 mA \times 12 kV), utilizing the 400 micron spot mode, which affords an elliptical analysis area of *ca* 400 \times 600 microns. Data were calibrated to the Ti 2p peak for the TiO₂ support (taken to be 458.8 eV) using an approach that avoids the uncertainties in calibration to the C1s signal, which can be affected by changes in the surface chemistry. Data were analysed using CasaXPS (v2.3.26 PR1.0N) [25]. Surface homogeneous equivalent concentrations were calculated using transmission-corrected spectra, with a combination of Scofield sensitivity factors and an electron escape depth according to the TPP-2M formulation after Shirley background subtraction. The chemical content of Au, Pd and Pt in the dried samples was achieved by microwave plasma-atomic emission spectroscopy (MP-AES). The metal catalysts were filtered and diluted to a metal concentration of approximately 10 ppm after being digested for 24 h (50 mg of catalyst and 5 ml of aqua regia). Metal concentrations were measured using an Agilent 4200 MP-AES 7900. Grams of metal per gram of material were used to express the metal weight loadings.

(c) Photocatalytic activity evaluation using visible light

The photocatalytic activity evaluation of the samples was performed in an open-air, glass photoreactor system containing 0.025 g of the catalyst and 50 ml of an aqueous solution of MO dye (10 ppm). The exposed-to-air suspension was kept at room temperature with no pH change (pH = 7), and with magnetic stirring at 350 r.p.m. A cold water bath was used to reduce thermal effects maintaining a temperature range between 25 and 30°C. The resultant solution was irradiated with visible light ($\lambda > 380$ nm; 68 mW cm⁻²) using a SOLIS-3C high-power LED lamp (Thorlabs) over 4 h. To guarantee the adsorption–desorption equilibrium, the suspension was held in the dark for 30 min prior to being exposed to visible light. The method used to measure the MO dye concentration in each case was to acquire a filtered aliquot of one millilitre at regular intervals, using a UV–vis spectrophotometer to measure the aliquot absorbance (with the MO dye absorption band at 464 nm).

Percentage degradation = $(1 C/C_0) \times 100$, where the MO solution absorbance maxima before and after the radiation period are denoted by C_0 and C , respectively. The Langmuir–Hinshelwood kinetic model, which is typically used to describe the photodegradation kinetics on semiconductors, was used to determine the reaction rate constant. Pseudo-first-order kinetics with an apparent first-order rate constant (k_{app}) can be used to simplify the reduction rate (r) in

cases where the adsorption or reactant concentration is low. The initial concentration (C_0) is the reactant concentration after reaching time (t), which can be expressed as

$$\ln(C/C_0) = -k_r k_{\text{ads}} C = -k_{\text{app}} t,$$

where k_r is the rate constant and k_{ads} is the adsorption equilibrium constant. The apparent rate constant (k_{app}) is the slope of a straight line obtained by plotting $\ln(C_0/C)$ against reaction time (t).

3. Results

(a) Structure of the photocatalysts

Figure 1 illustrates the XRD patterns of N-doped support decorated with Pd, Pt and Au. They were all showing signs the presence the anatase polymorph with reflections at 25.3° (101), 36.9° (103), 37.8° (004), 38.6° (112), 48.1° (200), 53.9° (105), 55.1° (204), 62.14° (213), 62.7° (204), 68.8° (116), 70.30° (220), 75.0° (215) and 76.0° (301), agreed with the JCPDS 01-075-2547 card; also the reflections related to the rutile phase at 27.4° (110), 36.1° (101), 41.3° (111) and 44.1° (210) agreed with the JCPDS 01-079-6031 card. No evidence of nitrogen was observed in the N-TiO₂ pattern. However, in the Pd/N-TiO₂ pattern, a reflection related to Pd (111) was identified according to matching JCPDS 01-087-0645. The absence of reflections correlating to Pt and Au phases in the XRD pattern of Pt/N-TiO₂ and Au/N-TiO₂ indicates that these metal particles are too small to be detected on the surface of N-TiO₂ surface. The crystallite size of the TiO₂ in each catalyst was determined using the Scherrer equation at $2\theta = 25.3^\circ$ (101) for the anatase phase and $2\theta = 27.4^\circ$ (110) for the rutile phase. The findings indicate that the addition of metallic nanoparticles on the surface of N-TiO₂ did not drastically affect the crystallite size for either phase, when compared to pristine P25 TiO₂, with the exception of Au/N-TiO₂ catalyst for rutile phase (see table 1). Figure 1b shows that the XRD reflections at $2\theta = 25.3^\circ$ for Pt and Au/N-TiO₂ catalyst are shifted to larger angles in comparison with pristine TiO₂. Table 1 indicates that for the materials, the measured loadings by MP-AES of Pd, Pt and Au metals were quite similar to the nominal one (1 wt%), indicating that DPU has good metal deposition efficiency.

(b) Textural properties

The values of the specific surface areas for N-TiO₂, Pd/N-TiO₂, Pt/N-TiO₂ and Au/N-TiO₂ catalysts were 56, 48, 63 and 95 m² g⁻¹, respectively. The specific surface area of N-TiO₂ did not drastically change, while for the Pd/N-TiO₂ catalyst it decreased with respect to pristine TiO₂-P25 (54 m² g⁻¹), probably as a result of Pd deposition causing partial occlusion of the support's pores. On the other hand, the deposition of Pt and Au increased the specific surface area of these compounds compared to the N-TiO₂ support, which was more evident in the Au/N-TiO₂ catalyst. The findings of the adsorption/desorption analysis for N-TiO₂, Pd/N-TiO₂, Pt/N-TiO₂ and Au/N-TiO₂ are shown in figure 2. All of the photocatalysts presented N₂ adsorption/desorption isotherm curves type IV with an H3-type hysteresis loop, indicating a distinctive mesoporous structure. The average pore sizes for the N-TiO₂, Pd/N-TiO₂, Pt/N-TiO₂ and Au/N-TiO₂ catalysts were 54.9, 17.9, 141 and 162 Å, respectively. A general trend was observed, with samples having a larger specific surface area also showing a larger pore size, probably owing to the influence of pH on the etching N-TiO₂ surface during the deposition precipitation method using urea [26,27].

Table 1. Textural properties of the compounds and their metal load.

catalyst	S_{BET} (m^2g^{-1})	average pore size (\AA)	crystallite size of anatase (nm)	crystallite size of rutile (nm)	anatase (101) peak position (2θ °)	d -spacing (nm)	actual M ($M =$ Pd, Pt or Au) content wt%
TiO ₂	54	45.1	21	31	25.3	35.1	—
N-TiO ₂	56	54.9	21	30	25.3	35.1	—
Pd/N-TiO ₂	48	17.9	21	31	25.3	35.2	1.2
Pt/N-TiO ₂	63	141	20	32	25.7	34.6	1.1
Au/N-TiO ₂	95	162	21	35	25.5	34.8	1.1

Metal loading determined by MP-AES.

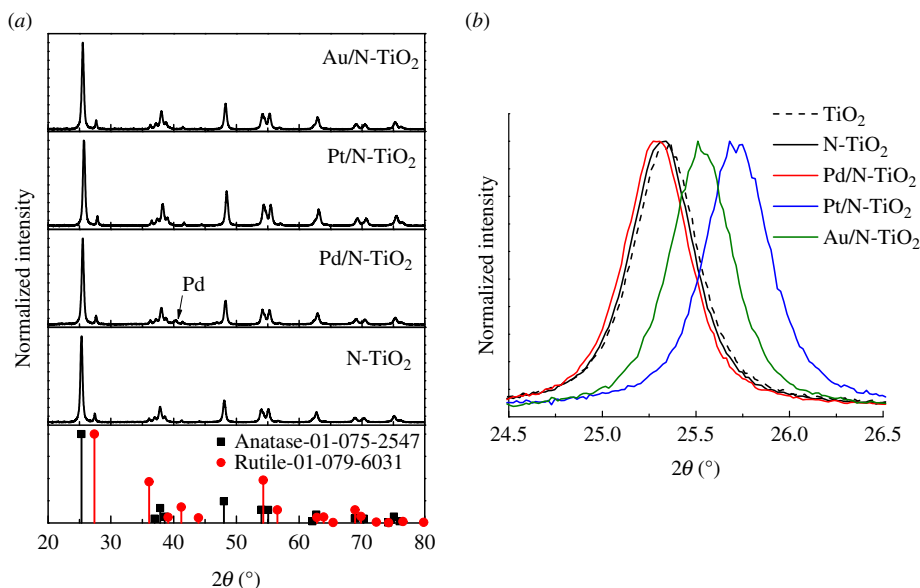


Figure 1. XRD pattern of (a) N-TiO₂, Pd/N-TiO₂, Pt/N-TiO₂ and Au/N-TiO₂ catalysts. (b) Magnified XRD peak at 25.3° (101) for all catalysts.

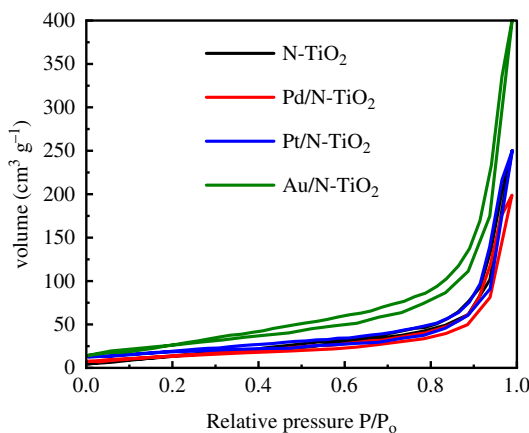


Figure 2. N₂ adsorption/desorption isotherms of N-TiO₂, Pd/N-TiO₂, Pt/N-TiO₂ and Au/N-TiO₂ catalysts.

(c) TEM and XPS

Figure 3a–c shows the TEM images and the associated dispersion of metal particle sizes for Pd/N-TiO₂, Pt/N-TiO₂ and Au/N-TiO₂ catalysts. Semi-spherical metallic nanoparticles of Pt and Au were well-dispersed on the N-TiO₂ surface with an average diameter of 3 and 2 nm, respectively. In contrast, the metallic nanoparticles of Pd were not as well dispersed on the support surface, with an average diameter of 6 nm and with a higher standard deviation (1.5) with respect to Pt and Au nanoparticles (0.5). These observations of particle size are in line with results from XPS, where the full-width-half-maximum of the nanoparticles are *ca.* 0.3–0.4 eV broader than their bulk metal equivalents (recorded under identical conditions) and have some differences in peak asymmetry for the Pt and Pd nanoparticles [28–30].

The surface elemental composition of the photocatalysts was studied using XPS to determine the extent of surface dopant inclusion. Table 2 lists the values for all the chemical elements

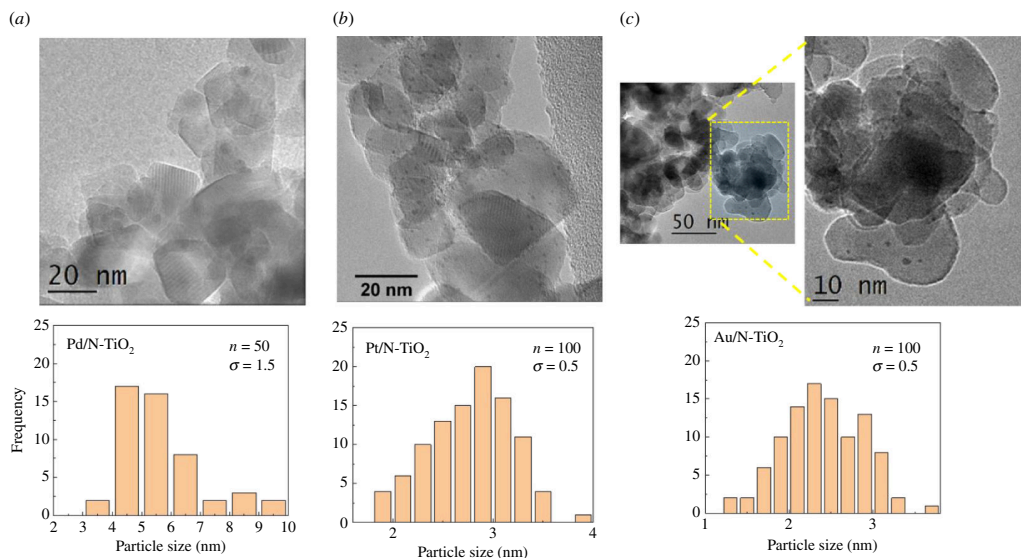


Figure 3. TEM images and particle size distribution for (a) Pd/N-TiO₂, (b) Pt/N-TiO₂ and (c) Au/N-TiO₂.

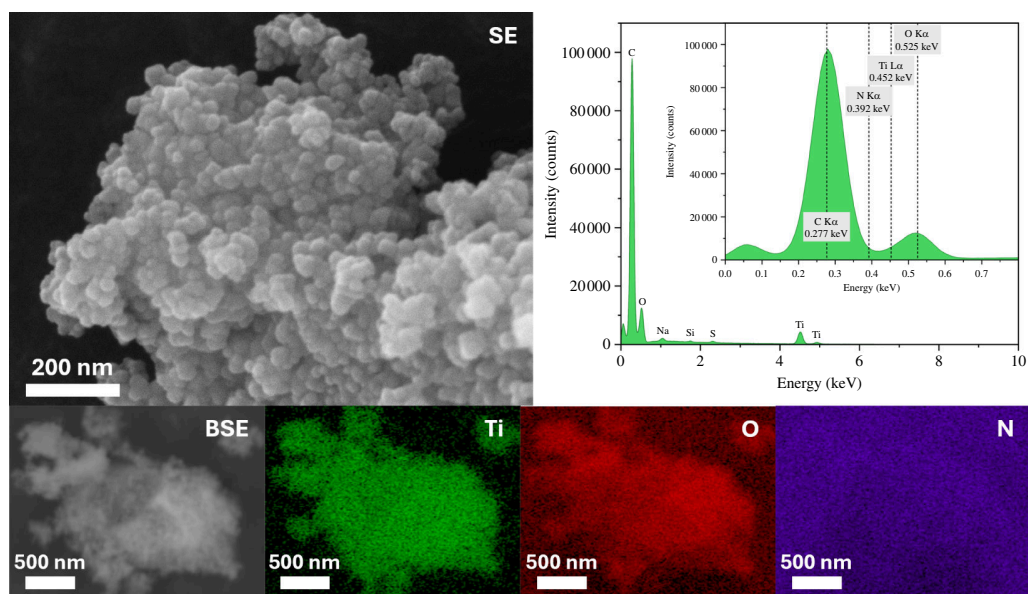


Figure 4. SEM imaging and EDX mapping of N-TiO₂. Secondary electron image taken at 250 kx. Backscattered electron image taken at 41 kx. Elemental maps show titanium, oxygen and nitrogen in area of BSE image, with EDX spectrum showing intensities of the elements detected.

present on the surface of the catalysts. In each case, nitrogen was observed. SEM-EDX was used to further investigate the existence of nitrogen in the catalysts. In contrast to the findings from XPS, nitrogen was not clearly observed by EDX in either N-TiO₂ (figure 4) or Au/N-TiO₂ (figure 5); however, this is believed to be due to the close overlap in the energies of the K α peaks for carbon (present from the adhesive carbon discs) and nitrogen, at 0.277 keV and 0.392 keV, respectively (see inset EDX spectrum). The presence of S is also explained by the adhesive used in the carbon discs, and Si is an artefact of the silicon drift detector used in EDX.

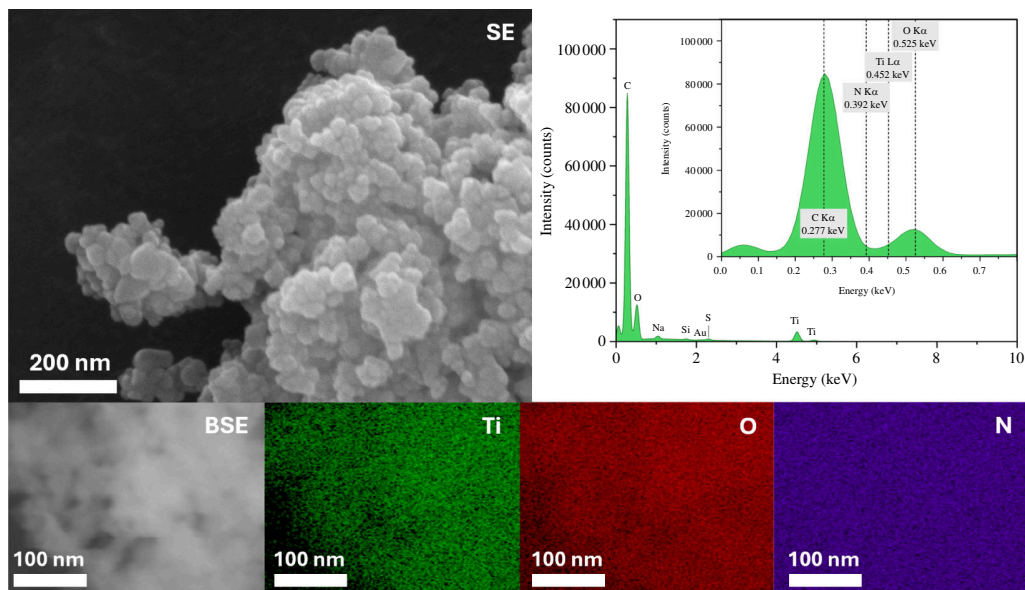


Figure 5. SEM imaging and EDX mapping of Au/N-TiO₂. Secondary electron image taken at 250 kx. Backscattered electron image taken at 320 kx. Elemental maps show titanium, oxygen and nitrogen in area of BSE image, with EDX spectrum showing intensities of the elements detected.

Table 2. Surface elemental composition of all catalysts as determined by XPS.

sample	C 1s (% atom)	N 1s (% atom)	O 1s (% atom)	Ti 2p (% atom)	Pd 3d (% atom)	Pt 4f (% atom)	Au 4f (% atom)
N-TiO ₂	27.9	0.29	50.67	21.13	—	—	—
Pd/N-TiO ₂	25.39	0.26	52.07	21.99	0.15	—	—
Pt/N-TiO ₂	26.04	0.19	51.78	21.67	—	0.18	—
Au/N-TiO ₂	25.74	0.26	52.27	21.41	—	—	0.18

(d) Diffuse reflectance spectroscopy (DRS)

Figure 6a shows the results of DRS of N-TiO₂, Pd/N-TiO₂, Pt/N-TiO₂ and Au/N-TiO₂ catalysts. The DRS of commercial TiO₂-P25 was also included as reference material. The band-gap energies of 3.2 and 3.0 eV, respectively, are associated with the well-known absorption of TiO₂ anatase and rutile phases, which are, respectively, approximately 387 and 413 nm in wavelength [31,32]. In comparison to TiO₂-P25, all of the surface-modified composites exhibited a shift in absorption to longer wavelengths, which was caused by the extra energy levels produced by N, Pd, Pt and Au on the surface of pristine TiO₂-P25. Additionally, the surface plasmon resonance (SPR) in the Au/N-TiO₂ photocatalyst reveals a unique behaviour concerning the absorption of gold nanoparticles in the visible spectrum (500–600 nm), verifying that the Au nanoparticles achieved the zero-valence state after being thermally treated in an H₂ environment [33]. The SPR phenomenon of metallic nanoparticles is dependent on several parameters, including the size, shape, loading and dielectric characteristics of the surrounding medium [34,35]. Optical band-gap (E_g) energies obtained from diffuse reflectance spectra are shown in figure 6b. The addition of nitrogen on the TiO₂-P25 surface helps to decrease its band gap from 3.18 to 2.9 eV. For Pd-, Pt- and Au-decorated photocatalysts, the reduction in band-gap energies was notably larger, measured at 2.86, 2.81 and 2.75 eV, respectively.

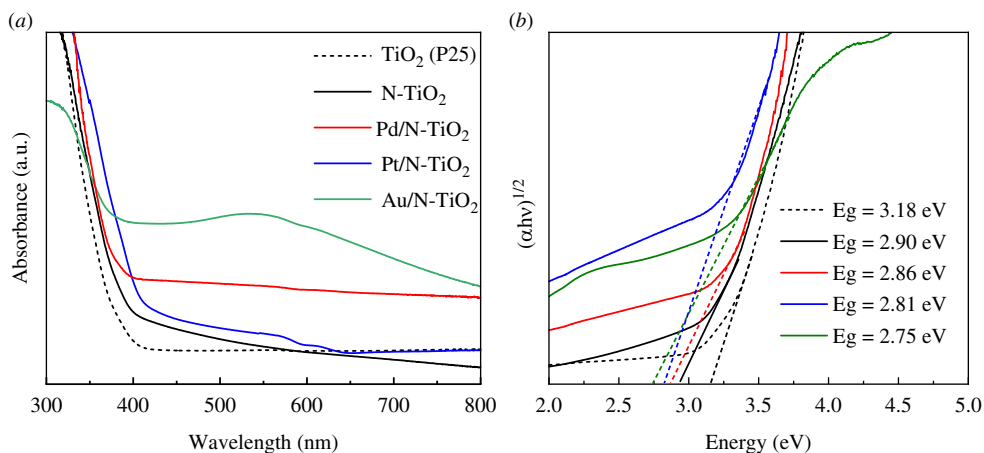


Figure 6. (a) Diffuse reflectance spectra and (b) diffuse absorbance spectra of the $(\alpha h\nu)^{1/2}$ plots for N-TiO₂, Pd/N-TiO₂, Pt/N-TiO₂, Au/N-TiO₂ and TiO₂-P25.

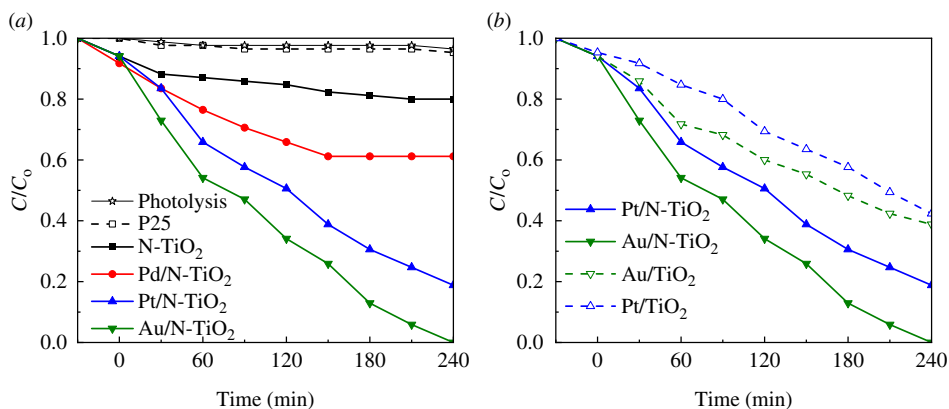


Figure 7. Evaluation of photocatalytic activity for (a) N-TiO₂, Pd/N-TiO₂, Pt/N-TiO₂, Au/N-TiO₂, TiO₂-P25 and (b) photocatalytic evaluation of compounds with and without nitrogen.

(e) Photocatalytic activity evaluation

Figure 7a shows the relative concentration profile (C/C_0) of the MO dye during both the photocatalytic and photolysis processes for TiO₂-P25, N-TiO₂, Pd/N-TiO₂, Pt/N-TiO₂, and Au/N-TiO₂ materials. The C/C_0 graphs show the initial dye concentration ($C/C_0 = 1$), the data were obtained after 30 min in darkness with stirring ($t = 0$), and the subsequent values are post-illumination because, as was previously noted, the adsorption–desorption equilibrium was reached after 30 min.

Under the visible light illumination conditions applied in this study, it is evident that the dye concentration remained unchanged during dark conditions, indicating negligible adsorption of the dye on to the powder surfaces. Furthermore, the photolysis exhibited only marginal decreases in the C/C_0 ratio, confirming the stability of the MO dye throughout the irradiation. This observation, coupled with the absence of dye adsorption on the powder surfaces and minimal photolysis, allows us to classify the decrease in time of the C/C_0 ratio as a discolouration process caused by photocatalytic activity in semiconductor materials, which is not the same as mineralization of the dye. Mineralization refers to the complete conversion of dye molecules to inorganic substances such as CO₂ and H₂O.

In the photocatalytic reaction using the TiO₂-P25, it was observed that the C/C_0 of the dye is very similar to the photolysis, which was expected owing to the value of its band gap (3.18 eV). In addition, the N-TiO₂ powder achieved a notable discolouration of the MO dye after 4 h. Incorporating Pd, Pt and Au nanoparticles on to the surface of N-TiO₂ notably enhanced its photocatalytic performance under visible light, culminating in complete discolouration of the MO dye by Au/N-TiO₂ within 4 h. Furthermore, as shown [figure 7b](#), the photocatalytic activity of Pt/N-TiO₂, Au/N-TiO₂, Pt/TiO₂ and Au/TiO₂ indicates that the combination of nitrogen and metallic nanoparticles on the TiO₂-P25 surface exhibited greater efficiency compared to the presence of metallic nanoparticles alone. This indicates a synergistic effect between the N and the Au/Pt. The apparent kinetic rate constants (K_{app}) calculated using the pseudo-first-order model for N-TiO₂, Pd/N-TiO₂, Pt/N-TiO₂ and Au/N-TiO₂ were 0.0007, 0.0028, 0.0054 and 0.0083 min⁻¹, respectively.

The stability of the best catalyst (Au/N-TiO₂) was tested by performing three consecutive cycles for MO dye degradation. The percentage value of MO dye degradation obtained in each cycle is shown in [figure 8](#). The sample was gathered and centrifuged following each cycle to assess its potential for reuse. The photodegradation efficacies of MO dye were 99.9, 89 and 73% for first, second and third cycles, respectively. The photodegradation effectiveness of the Au/N-TiO₂ catalyst was diminished as the cycle number increased; powder loss during suspension and centrifugation treatment may be the primary cause of this.

4. Discussion

In this work, nitrogen and metallic nanoparticles (Pd, Pt and Au) were used to modify commercial TiO₂-P25 and to improve its photocatalytic performance under visible light to degrade the MO dye. Interestingly, these combinations (metal and non-metal) have been used to enhance visible light absorption of TiO₂ previously [6]. The findings of this investigation reveal that the best photocatalyst for MO dye degradation under visible light illumination was the Au/N-TiO₂ composite, followed in effectiveness by the Pt/N-TiO₂ composite, with the least effective catalyst being the Pd/N-TiO₂ composite.

The improved photocatalytic activity, using visible light illumination, of the Pt/N-TiO₂ and Au/N-TiO₂ photocatalysts is associated with their fundamental physical characteristics. It is commonly recognized that photocatalysts with large surface areas and/or small crystal sizes exhibit enhanced photocatalytic performance when it comes to the breakdown of organic compounds. The results demonstrate that the inclusion of all dopants on the TiO₂-P25 increased the surface area in all cases except for palladium. The largest increase in surface area was from 54 to 95 m² g⁻¹ for Au/N-TiO₂, while the crystalline sizes did not change with the addition of N, Pd, Pt or Au with respect to bare TiO₂. Furthermore, the increased size and well-defined mesoporous structure of the Pt and Au catalysts enabled MO molecules (6–8 nm) to transfer and diffuse into the interior pores (14.1 nm for Pt/N-TiO₂ and 16.2 nm for Au/N-TiO₂), thus increasing the MO-photocatalyst contact interface and providing more reactive sites, resulting in an increase of MO dye degradation. The majority of previous research has concentrated on metallic nanoparticles with sizes ranging from 5 to 100 nm and found that as size decreased, catalytic activity increased [36–42]. On a few occasions, nanoparticle catalytic activity may decrease with decreasing size or remain unchanged [43,44]. It has been shown that small gold nanoclusters (<1.5 nm) exhibit a quantized electronic structure similar to a molecule owing to the quantum confinement phenomenon [45,46]. In this study, the nanoparticle sizes obtained were 5, 3 and 2 nm for Pd, Pt and Au, respectively.

All the diffraction patterns exhibited both the anatase and rutile phases related to commercial TiO₂-P25 except the Pd/N-TiO₂ material, where one small reflection was observed indicating the presence of metallic Pd. This observation suggests a larger particle size for Pd nanoparticles compared to the Pt and Au. [Figure 1b](#) shows that in comparison to TiO₂-P25, the XRD reflections of Pt/N-TiO₂ and Au/N-TiO₂ are displaced to higher angles, indicating a lattice

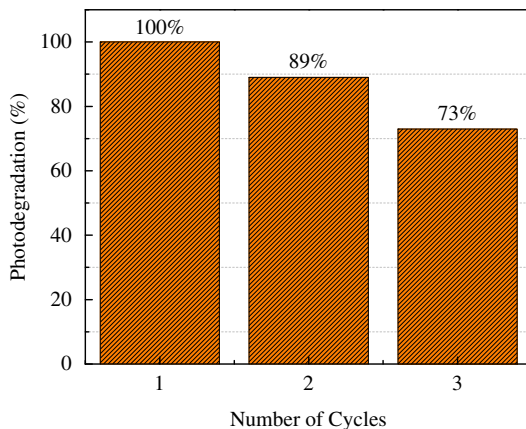


Figure 8. Percentage degradation values of MO dye obtained from the stability test using Au/TiO₂ catalyst.

contraction. The synergy observed between Pt and Au ions with TiO₂ is undoubtedly crucial, given that doped titania reveals diverse benefits to its photocatalytic activities by modifying its surface features and reducing the band gap. This agrees with the estimated optical band-gap (E_g) energies obtained from DRS for all materials that suffered a decrease with respect to E_g values for bare TiO₂. Specifically, Ti 3d and O 2p orbitals constitute the majority of the conduction and valence bands in the TiO₂ matrix [47,48]. Introducing additional metal ions into the structure of TiO₂ leads to interactions between the outer shell orbitals of these ions and the energy states in the bands, resulting in the creation of impurity levels and alterations in the band structures. Indeed, the influence of dopants on the electronic structures of semiconductors is closely linked to several factors, including the dopant atomic numbers, ionic radii and oxidation states [2,17,48]. These characteristics determine the extent of modifications in the band structure, impurity levels and, ultimately, the photocatalytic performance of the doped material. In summary, the presence of Pt and Au nanoparticles on the N-TiO₂ surface leads to a significant distortion of the octahedral geometry, causing the conduction-band minimum to shift downward to lower energy levels, modifying its electronic properties and catalytic behaviour.

The surface chemical composition was obtained using XPS (table 2). It is important to emphasize that in each case nitrogen was detected on the surface of the TiO₂-P25, and so we propose the near-surface is N functionalized, which, with a nitrogen binding energy of 399.7 eV, is characteristic of NH_x species; however, the insertion of nitrogen at interstitial sites cannot be excluded [49]. Studies have demonstrated that co-catalysts (metallic nanoparticles) and N-functionalized TiO₂ surfaces can form strong complexes with N bound on the surface, increasing loading levels and reducing co-catalyst agglomeration [18,50–52]. This can be seen in figure 5b, where the photocatalytic activity of the composites with N and Pt or Au nanoparticles presents much better photocatalytic performance than the composites with only Pt or Au nanoparticles on the surface, suggesting a synergistic effect between N and metallic nanoparticles.

There are some reports related to the use of non-metal and metal ions to improve the photocatalytic efficiency of TiO₂ for dye degradation [4,53,54]. Nonetheless, the Au/N-TiO₂ photocatalyst prepared in this study showed comparable or even better photocatalytic performance for MO dye degradation than those reported in previous works (table 3) without altering the pH, adding H₂O₂ or using UV illumination. The apparent kinetic rate constant (k_{app}) for the Au/N-TiO₂ photocatalyst was 0.0083 min⁻¹, which is more than ten times larger than the K_{app} of N-TiO₂ composite (0.0007 min⁻¹), two times larger than that estimated by Kader *et al.* [59] (0.004 min⁻¹) and more than five times larger than the one reported by Ellouzi *et al.* [53] (0.0015 min⁻¹) under similar experimental conditions. However, it is important to mention that the lack of standardization makes it difficult to reliably compare and

Table 3. A comparison of the photocatalytic activity between the current study and other published works.

material	dye	catalyst amount (g)	dye conc. (ppm)	pH	type of light	illumination time (min)	effectiveness (%)	ref.
TiO ₂ -NPs/MO	MO	0.15	15	3	100 W UV lamp	300	99.8	[55]
TiO ₂ -NPs	MO	0.10	5	—	182 W UV lamp	240	41.1	[56]
TiO ₂ spheres	MO	0.02	10	7	32 W Hg lamp	140	89.7	[57]
TiO ₂ /ASS	MO	0.2	25	7	UV lamp	360	90	[58]
Ag/MoO ₃ /TiO ₂	MO	0.12	10	7	UV irradiation	330	75.8	[59]
C, N, S-Fe-TiO ₂	MO	0.5	10	—	6 W visible lamp	180	25	[53]
M/TiO ₂ (M = Mn, Ni, Co)	MO	—	8	—	300 W lamp that simulates solar radiation	600	60	[60]
NiSO ₄ /TiO ₂	MO	1 g l ⁻¹	10	5.8	UV irradiation	120	31	[54]
TiO ₂ -Ag-WO ₃	methylene blue	0.5	10	7	121 W visible light source	60	72	[61]
TiO ₂ -Au-WO ₃	methylene blue	0.02	30	—	300 W xenon lamps	240	94.5	[62]
TiO ₂ -F-WO ₃	MO	0.12	10	3	100 W UV irradiation	330	99.68	[63]
Au/N-TiO ₂	MO	0.025	10	7	visible light	240	99.9	this work

reproduce findings across photocatalytic studies. Kisch & Bahnemann [64] suggest that for solid/liquid photocatalytic systems, an apparent optimal quantum yield should be obtained, which improves the comparability of photocatalytic activity results across different laboratories.

5. Conclusion

This work demonstrates that doping TiO₂ with nitrogen and metallic nanoparticles (Pd/N-TiO₂, Pt/N-TiO₂ and Au/N-TiO₂) enhances the photocatalytic decomposition of MO mediated by visible light. The optimum photocatalytic activity in MO dye degradation was achieved using Au/N-TiO₂ photocatalyst with 99.9% degradation observed after 4 h with an apparent first-order constant rate of $k_{app} = 0.0083 \text{ min}^{-1}$. The photocatalytic performance during visible light illumination of Au/N-TiO₂ with respect to the other composites is explained by the well-dispersed and smaller nanoparticle size (2 nm), largest surface area (95 m²g⁻¹, 1.7 times larger than bare TiO₂), lowest band-gap energy (2.75 eV) and synergistic effect at the interface sites between N and Au nanoparticles, with all of these confirmed by XRD, TEM, BET, DRS and XPS characterization techniques.

Data accessibility. Information on the data underpinning the results presented here, including how to access them, can be found in the Cardiff University data catalogue at [65].

Declaration of AI use. We have not used AI-assisted technologies in creating this article.

Authors' contributions. J.C.M.: conceptualization, data curation, investigation, methodology, writing—original draft; E.W.: conceptualization, investigation, methodology; D.M.: data curation, formal analysis, investigation, methodology, writing—original draft; I.E.G.: formal analysis, investigation, writing—original draft; J.E.: conceptualization, formal analysis, funding acquisition, methodology, project administration, supervision, writing—original draft, writing—review and editing.

All authors gave final approval for publication and agreed to be held accountable for the work performed therein.

Conflict of interests. We declare we have no competing interests.

Funding. This work was supported, in whole or in part, by the Bill & Melinda Gates Foundation (INV-048434). Under the grant conditions of the Foundation, a Creative Commons Attribution 4.0 Generic License has already been assigned to the Author Accepted Manuscript version that might arise from this submission.

Acknowledgements. J.K.E. would like to acknowledge the Harmonized Impact Acceleration Account for Funding IG and Sêr Cymru programme, Welsh Government for the provision of the solar simulator. This publication is based on research funded by (or in part by) the Bill & Melinda Gates Foundation. The findings and conclusions contained within are those of the authors and do not necessarily reflect positions or policies of the Bill & Melinda Gates Foundation.

X-ray photoelectron (XPS) data were acquired at the EPSRC National Facility for XPS ('HarwellXPS', EP/Y023587/1, EP/Y023609/1, EP/Y023536/1, EP/Y023552/1 and EP/Y023544/1).

For the purpose of open access, the author has applied a CC BY public copyright license (where permitted by UKRI, 'Open Government License' or 'CC BY-ND public copyright license' may be stated instead) to any Author Accepted Manuscript version arising.

References

1. Fujishima A, Honda K. 1972 Electrochemical photolysis of water at a semiconductor electrode. *Nature* **238**, 37–38. (doi:10.1038/238037a0)
2. Chang S m., Liu W s. 2014 The roles of surface-doped metal ions (V, Mn, Fe, Cu, Ce, and W) in the interfacial behavior of TiO₂ photocatalysts. *Appl. Catal. B: Environ.* **156–157**, 466–475. (doi:10.1016/j.apcatb.2014.03.044)
3. Li D, Song H, Meng X, Shen T, Sun J, Han W, Wang X. 2020 Effects of particle size on the structure and photocatalytic performance by alkali-treated TiO(2). *Nanomaterials* **10**, 546. (doi:10.3390/nano10030546)
4. Muscetta M, Jitan SA, Palmisano G, Andreozzi R, Marotta R, Cimino S, Di Somma I. 2022 Visible light – driven photocatalytic hydrogen production using Cu₂O/TiO₂ composites

- prepared by facile mechanochemical synthesis. *J. Environ. Chem. Eng.* **10**, 107735. (doi:10.1016/j.jece.2022.107735)
5. Devi LG, Kavitha R. 2013 A review on non metal ion doped titania for the photocatalytic degradation of organic pollutants under UV/solar light: role of photogenerated charge carrier dynamics in enhancing the activity. *Appl. Catal. B Environ.* **140–141**, 559–587. (doi:10.1016/j.apcatb.2013.04.035)
 6. Nagaveni K, Hegde MS, Madras G. 2004 Structure and photocatalytic activity of TiMO (M = W, V, Ce, Zr, Fe, and Cu) synthesized by solution combustion method. *J. Phys. Chem. B* **108**, 20204–20212. (doi:10.1021/jp047917v)
 7. Reza KM, Kurny ASW, Gulshan F. 2017 Parameters affecting the photocatalytic degradation of dyes using TiO₂: a review. *Appl. Water Sci.* **7**, 1569–1578. (doi:10.1007/s13201-015-0367-y)
 8. Habib IY, Burhan J, Jaladi F, Lim CM, Usman A, Kumara NTRN, Tsang SCE, Mahadi AH. 2021 Effect of Cr doping in CeO₂ nanostructures on photocatalysis and H₂O₂ assisted methylene blue dye degradation. *Catal. Today* **375**, 506–513. (doi:10.1016/j.cattod.2020.04.008)
 9. Ansari M, Sajjadi SA, Sahebani S, Heidari EK. 2020 Photocatalytic and antibacterial activity of silver/titanium dioxide/zinc oxide nanoparticles coated on cotton fabrics. *ChemistrySelect* **5**, 8370–8378. (doi:10.1002/slct.202001655)
 10. Calzada LA, Louis C, Wan Han C, Ortalan V, Zanella R. 2020 Au-Ru/TiO₂ prepared by deposition-precipitation with urea: relevant synthesis parameters to obtain bimetallic particles. *Appl. Catal. B Environ.* **264**, 118503. (doi:10.1016/j.apcatb.2019.118503)
 11. Padikkaparambil S, Narayanan B, Yaakob Z, Viswanathan S, Tasirin SM. 2013 Au/TiO₂ reusable photocatalysts for dye degradation. *Int. J. Photoenergy* **2013**, 1–10. (doi:10.1155/2013/752605)
 12. Yang J *et al.* 2023 Enhancing visible-light photocatalytic performance of Au/TiO₂ catalysts through light reflection-promoted optical absorption with oriented anatase mesocrystals. *J. Mater. Chem. A* **11**, 4751–4757. (doi:10.1039/D2TA09982A)
 13. Kim S, Hwang SJ, Choi WY. 2005 Visible light active platinum-ion-doped TiO₂ photocatalyst. *J. Phys. Chem. B* **109**, 24260–24267. (doi:10.1021/jp055278y)
 14. Nguyen CH, Fu CC, Juang RS. 2018 Degradation of methylene blue and methyl orange by palladium-doped TiO₂ photocatalysis for water reuse: efficiency and degradation pathways. *J. Clean. Prod.* **202**, 413–427. (doi:10.1016/j.jclepro.2018.08.110)
 15. Nkambule TI, Kuvarega AT, Krause RWM, Haarhoff J, Mamba BB. 2012 Synthesis and characterisation of Pd-modified N-doped TiO₂ for photocatalytic degradation of natural organic matter (NOM) fractions. *Environ. Sci. Pollut. Res.* **19**, 4120–4132. (doi:10.1007/s11356-012-0872-6)
 16. Seery MK, George R, Floris P, Pillai SC. 2007 Silver doped titanium dioxide nanomaterials for enhanced visible light photocatalysis. *J. Photochem. Photobiol. A Chem.* **189**, 258–263. (doi:10.1016/j.jphotochem.2007.02.010)
 17. Camposeco R, Hinojosa-Reyes M, Zanella R. 2022 Behavior of the energy levels of hydrogen titanate nanotubes decorated with Au, Ag, Mn, and Ni and their effect on the H₂ evolution. *Top. Catal.* **65**, 989–999. (doi:10.1007/s11244-022-01639-w)
 18. Motamedisade A, Heydari A, Yin YT, Alotabi AS, Andersson GG. 2024 Enhanced photocatalytic degradation of methyl orange using nitrogen-functionalized mesoporous TiO₂ decorated with Au₉ nanoclusters. *Sol. Rrl.* (doi:10.1002/solr.202300943)
 19. Clark JH, Dyer MS, Palgrave RG, Ireland CP, Darwent JR, Claridge JB, Rosseinsky MJ. 2011 Visible light photo-oxidation of model pollutants using CaCu₃Ti₄O₁₂: an experimental and theoretical study of optical properties, electronic structure, and selectivity. *J. Am. Chem. Soc.* **133**, 1016–1032. (doi:10.1021/ja1090832)
 20. Zhang B, Li X, Akiyama K, Bingham PA, Kubuki S. 2022 Elucidating the mechanistic origin of a spin state-dependent FeN_x-C catalyst toward organic contaminant oxidation via peroxymonosulfate activation. *Environ. Sci. Technol.* **56**, 1321–1330. (doi:10.1021/acs.est.1c05980)
 21. Asahi R, Morikawa T, Irie H, Ohwaki T. 2014 Nitrogen-doped titanium dioxide as visible-light-sensitive photocatalyst: designs, developments, and prospects. *Chem. Rev.* **114**, 9824–9852. (doi:10.1021/cr5000738)

22. Bakar SA, Ribeiro C. 2016 Nitrogen-doped titanium dioxide: an overview of material design and dimensionality effect over modern applications. *J. Photochem. Photobiol. C Photochem. Rev.* **27**, 1–29. (doi:10.1016/j.jphotochemrev.2016.05.001)
23. Schneider J, Matsuoka M, Takeuchi M, Zhang J, Horiuchi Y, Anpo M, Bahnemann DW. 2014 Understanding TiO₂ photocatalysis: mechanisms and materials. *Chem. Rev.* **114**, 9919–9986. (doi:10.1021/cr5001892)
24. Daghrir R, Drogui P, Robert D. 2013 Modified TiO₂ for environmental photocatalytic applications: a review. *Ind. Eng. Chem. Res.* **52**, 3581–3599. (doi:10.1021/ie303468t)
25. Fairley N *et al.* 2021 Systematic and collaborative approach to problem solving using X-ray photoelectron spectroscopy. *Appl. Surf. Sci. Adv.* **5**, 100112. (doi:10.1016/j.apsadv.2021.100112)
26. Liu H, Bansal S. 2023 Metal halide perovskite nanostructures and quantum dots for photocatalytic CO₂ reduction: prospects and challenges. *Mat. Today Energy* **32**, 101230. (doi:10.1016/j.mtener.2022.101230)
27. García-Domínguez ÁE, Torres-Torres G, Arévalo-Pérez JC, Silahua-Pavón A, Sánchez-Trinidad C, Godavarthi S, Ojeda-López R, Sierra-Gómez UA, Cervantes-Urbe A. 2022 Urea assisted synthesis of TiO₂-CeO₂ composites for photocatalytic acetaminophen degradation via simplex-centroid mixture design. *Res. Eng.* **14**, 100443. (doi:10.1016/j.rineng.2022.100443)
28. Wertheim GK. 1987 Core-electron binding energies in free and supported metal clusters. *Z. Physik B Condensed Matter* **66**, 53–63. (doi:10.1007/BF01312762)
29. Morgan DJ. 2023 XPS insights: asymmetric peak shapes in XPS. *Surf. Interface Anal.* **55**, 567–571. (doi:10.1002/sia.7215)
30. Cheung TTP. 1986 X-ray photoemission studies of Pt-Sn and Pt-Pb bimetallic systems. *Surf. Sci.* **177**, 493–514. (doi:10.1016/0039-6028(86)90029-4)
31. Jang HD, Kim SK, Kim SJ. 2001 Effect of particle size and phase composition of titanium dioxide nanoparticles on the photocatalytic properties. *J. Nanopart. Res.* **3**, 141–147. (doi:10.1023/A:1017948330363)
32. Scanlon DO *et al.* 2013 Band alignment of rutile and anatase TiO₂. *Nat. Mater.* **12**, 798–801. (doi:10.1038/nmat3697)
33. Medina JC, Garcia-Perez VI, Zanella R. 2021 Metallic composites based on Ag, Cu, Au and Ag-Cu nanoparticles with distinctive bactericidal effect on varied species. *Mat. Today. Commun.* **26**, 102182. (doi:10.1016/j.mtcomm.2021.102182)
34. Dodekatos G, Schünemann S, Tüysüz H. 2016 Surface plasmon-assisted solar energy conversion. In *Solar energy for fuels* (eds J H. Tüysüz, CK Chan), pp. 215–252. Cham: Springer International Publishing. (doi:10.1007/128_2015_642)
35. Du LC, Furube A, Yamamoto K, Hara K, Katoh R, Tachiya M. 2009 Plasmon-induced charge separation and recombination dynamics in gold-TiO₂ nanoparticle systems: dependence on TiO₂ particle size. *J. Phys. Chem. C.* **113**, 6454–6462. (doi:10.1021/jp810576s)
36. Jin RC, Li G, Sharma S, Li YW, Du XS. 2021 Toward active-site tailoring in heterogeneous catalysis by atomically precise metal nanoclusters with crystallographic structures. *Chem. Rev.* **121**, 567–648. (doi:10.1021/acs.chemrev.0c00495)
37. Du YX, Sheng HT, Astruc D, Zhu MZ. 2020 Atomically precise noble metal nanoclusters as efficient catalysts: a bridge between structure and properties. *Chem. Rev.* **120**, 526–622. (doi:10.1021/acs.chemrev.8b00726)
38. Li S, Du X, Liu Z, Li Y, Shao Y, Jin R. 2023 Size effects of atomically precise gold nanoclusters in catalysis. *Precis. Chem.* **1**, 14–28. (doi:10.1021/prechem.3c00008)
39. Li Y, Zhang P, Wan D, Xue C, Zhao J, Shao G. 2020 Direct evidence of 2D/1D heterojunction enhancement on photocatalytic activity through assembling MoS₂ nanosheets onto super-long TiO₂ nanofibers. *Appl. Surf. Sci.* **504**, 144361. (doi:10.1016/j.apsusc.2019.144361)
40. Dong C, Lian C, Hu S, Deng Z, Gong J, Li M, Liu H, Xing M, Zhang J. 2018 Size-dependent activity and selectivity of carbon dioxide photocatalytic reduction over platinum nanoparticles. *Nat. Commun.* **9**, 1252. (doi:10.1038/s41467-018-03666-2)
41. Raza MA, Kanwal Z, Rauf A, Sabri AN, Riaz S, Naseem S. 2016 Size- and shape-dependent antibacterial studies of silver nanoparticles synthesized by wet chemical routes. *Nanomaterials* **6**, 74. (doi:10.3390/nano6040074)
42. Ydollahi M, Ahari H, Anvar AA. 2016 Antibacterial activity of silver-nanoparticles against staphylococcus aureus. *Afr. J. Microbiol. Res.* **10**, 850–855. (doi:10.5897/AJMR2016.7908)

43. Seong H, Efremov V, Park G, Kim H, Yoo JS, Lee D. 2021 Atomically precise gold nanoclusters as model catalysts for identifying active sites for electroreduction of CO₂ *Angew. Chem. Int. Ed. Engl.* **60**, 14563–14570. (doi:10.1002/anie.202102887)
44. Li S, Nagarajan AV, Du X, Li Y, Liu Z, Kauffman DR, Mpourmpakis G, Jin R. 2022 Dissecting critical factors for electrochemical CO₂ reduction on atomically precise Au nanoclusters. *Angew. Chem. Int. Ed.* **61**, e202211771. (doi:10.1002/anie.202211771)
45. Adnan RH, Madridejos JML, Alotabi AS, Metha GF, Andersson GG. 2022 A review of state of the art in phosphine ligated gold clusters and application in catalysis. *Adv. Sci. (Weinh.)* **9**, e2105692. (doi:10.1002/advs.202105692)
46. Mousavi H, Yin Y, Howard-Fabretto L, Sharma SK, Golovko V, Andersson GG, Shearer CJ, Metha GF. 2021 Au₁₀₁-rGo nanocomposite: immobilization of phosphine-protected gold nanoclusters on reduced graphene oxide without aggregation. *Nanoscale Adv.* **3**, 1422–1430. (doi:10.1039/d0na00927j)
47. Kreibitz U, Vollmer M. 1995 Optical properties of metal clusters. *Springer Ser. Mater. Sci.* **25**, 535. (doi:10.1007/978-3-662-09109-8)
48. Shough AM, Doren DJ, Ogunnaike B. 2009 Transition metal substitution in ETS-10: DFT calculations and a simple model for electronic structure prediction. *Chem. Mater.* **21**, 1232–1241. (doi:10.1021/cm8021177)
49. Dunnill CWH, Aiken ZA, Pratten J, Wilson M, Morgan DJ, Parkin IP. 2009 Enhanced photocatalytic activity under visible light in N-doped TiO₂ thin films produced by APCVD preparations using T-butylamine as a nitrogen source and their potential for antibacterial films. *J. Photochem. Photobiol. A* **207**, 244–253. (doi:10.1016/j.jphotochem.2009.07.024)
50. Kitazawa N, Sato H, Watanabe Y. 2007 Effects of post-deposition chemical treatment on the formation of mesoporous titania films. *J. Mater. Sci.* **42**, 5074–5079. (doi:10.1007/s10853-006-0479-8)
51. Martínez - Ferrero E, Sakatani Y, Boissière C, Grosso D, Fuertes A, Fraxedas J, Sanchez C. 2007 Nanostructured titanium oxynitride porous thin films as efficient visible - active photocatalysts. *Adv. Funct. Mater.* **17**, 3348–3354. (doi:10.1002/adfm.200700396)
52. Viswanathan B, Krishnamurthy KR. 2012 Nitrogen incorporation in TiO₂: does it make a visible light photo-active material?. *Int. J. Photoenergy* **2012**, 1–10. (doi:10.1155/2012/269654)
53. Ellouzi I, El Hajjaji S, Harir M, Schmitt Koplin P, Robert D, Laânab L. 2019 Synergistic effects of C, N, S, Fe-multidoped TiO₂ for photocatalytic degradation of methyl orange dye under UV and visible light irradiations. *SN Appl. Sci.* **1**. (doi:10.1007/s42452-019-0857-x)
54. Regraguy B, Rahmani M, Mabrouki J, Drhimer F, Ellouzi I, Mahmoud C, Dahchour A, Mrabet ME, Hajjaji SE. 2022 Photocatalytic degradation of methyl orange in the presence of nanoparticles NiSO₄/TiO₂. *Nanotechnol. Environ. Eng.* **7**, 157–171. (doi:10.1007/s41204-021-00206-0)
55. Rashid Al-Mamun M, Hossain KT, Mondal S, Afroza Khatun M, Shahinoor Islam M, Zaved Hossain Khan DM. 2022 Synthesis, characterization, and photocatalytic performance of methyl orange in aqueous TiO₂ suspension under UV and solar light irradiation. *S. Afr. J. Chem. Eng.* **40**, 113–125. (doi:10.1016/j.sajce.2022.02.002)
56. Mosquera EE, Herrera-Molina D, Diosa JE. 2021 Propiedades estructurales y ópticas de las nanopartículas de TiO₂ y su comportamiento fotocatalítico bajo luz visible. *Ing. Compet.* **23**, e21310965. (doi:10.25100/iyv.v23i2.10965)
57. Kanjana N, Maiaugree W, Poolcharuansin P, Laokul P. 2020 Size controllable synthesis and photocatalytic performance of mesoporous TiO₂ hollow spheres. *J. Mater. Sci. Technol.* **48**, 105–113. (doi:10.1016/j.jmst.2020.03.013)
58. Rashed MN, Eltaher MA, Abdou ANA. 2017 Adsorption and photocatalysis for methyl orange and Cd removal from wastewater using TiO₂. *R. Soc. Open Sci.* **4**, 170834. (doi:10.1098/rsos.170834)
59. Kader S, Al-Mamun MR, Suhan MBK, Shuchi SB, Islam MS. 2022 Enhanced photodegradation of methyl orange dye under UV irradiation using MoO₃ and Ag doped TiO₂ photocatalysts. *Environ. Technol. Inno.* **27**, 102476. (doi:10.1016/j.eti.2022.102476)
60. Stojadinović S, Radić N, Vasilić R, Tadić N, Tsanev A. 2022 Photocatalytic degradation of methyl orange in the presence of transition metals (Mn, Ni, Co) modified TiO₂ coatings formed by plasma electrolytic oxidation. *Solid State Sci.* **129**, 106896. (doi:10.1016/j.solidstatesciences.2022.106896)

61. Basumatary B, Basumatary R, Ramchiary A, Konwar D. 2022 Evaluation of Ag@TiO₂/Wo₃ heterojunction photocatalyst for enhanced photocatalytic activity towards methylene blue degradation. *Chemosphere* **286**, 131848. (doi:10.1016/j.chemosphere.2021.131848)
62. Yang X, Fu H, Wang W, Xiong S, Han D, Deng Z, An X. 2020 Enhanced solar light photocatalytic performance based on a novel Au-WO₃@TiO₂ ternary core-shell nanostructures. *Appl. Surf. Sci.* **505**, 144631. (doi:10.1016/j.apsusc.2019.144631)
63. Suhan MBK, Shuchi SB, Al-Mamun MR, Roy H, Islam MS. 2023 Enhanced UV light-driven photocatalytic degradation of methyl orange using MoO₃/WO₃-fluorinated TiO₂ nanocomposites. *Environ. Nanotechnol. Monit. Manag.* **19**, 100768. (doi:10.1016/j.enmm.2022.100768)
64. Kisch H, Bahnemann D. 2015 Best practice in photocatalysis: comparing rates or apparent quantum yields? *J. Phys. Chem. Lett.* **6**, 1907–1910. (doi:10.1021/acs.jpcllett.5b00521)
65. Gow I, Morgan D, Medina JC *et al.* 2024 Influence of Pd, Pt, and Au nanoparticles in the photocatalytic activity of N-TiO₂ support under visible light: Data. Cardiff University (doi:10.17035/d.2024.0316533542)